Analysis of Coherent Gradient Sensing (CGS) by Fourier Optics

Yeong Joo Lee, John Lambros* & Ares J. Rosakis

Graduate Aeronautical Laboratories, California Institute of Technology, Pasadena,
CA 91125, USA

ABSTRACT

A coherent laser beam reflected or transmitted from a deforming plate specimen acquires an optical path difference (phase change) which is related to the deformation and stress field. The optical method of Coherent Gradient Sensing (CGS) uses two parallel grating plates to displace (shear) and recombine the distorted light beam emerging from the specimen. Fringes are produced on the image plane by the interference of the shifted and unshifted beams. The fringe pattern is related to the spatial difference of the phase in the shearing direction. If the shearing distance is small enough, the spatial difference of the phase approximates to its gradient. Each fringe in the image represents a locus of equal gradient component of the phase in the shearing direction. The technique is interpreted by means of wave optics, using the Fraunhofer approximation and the paraxial theory of lenses. The assumptions made in earlier analyses have been removed here. A more precise analysis based on Fourier optics is presented. The simplicity of the optical setup and variable resolution of the technique have led to its frequent use in the area of solid mechanics, including fracture mechanics. Some examples are discussed in the second half of this paper.

1 INTRODUCTION

Coherent Gradient Sensing (CGS) is an optical technique based on lateral shearing and interference of a coherent laser beam. Image

---

* Current address: Mechanical Engineering Department, University of Delaware, Newark, DE 19716, USA.

shearing and interference have been frequently used in various optical techniques in the past. Bates,[1] for instance, modified the arrangement of the Mach–Zehnder interferometer[2] by rotating one of the beam splitters in the optical setup. The purpose was to measure the asphericity of convergent wave fronts without the need for a substantially error-free reference wave front, such as is required for the Twyman–Green interferometer.[2] Lateral shearing interferometry has been accomplished in the past by using several different optical tools to perform the beam shearing action. These could be beam splitters,[3] Wallestone prisms[4] or two diffraction gratings.[5,6] Double grating interferometry, the later of the above methods, has been used by Hariharan et al.[5] and Hariharan and Hegedus[6] to measure lens aberrations. The proposed CGS setup is a modification of the above setup that uses two very fine gratings, in conjunction with spatial filtering, to produce lateral shearing that leads to interference fringes.

In particular in fracture mechanics experiments, the methods of photoelasticity,[7] caustics,[8,9] geometric moiré and moiré interferometry,[10,11] and the stress intensity factor tracer,[12] have been frequently used to measure crack tip deformations and fracture parameters. However, each method has certain disadvantages. The method of caustics and the stress intensity factor tracer, for example, do not perform full field measurements, while photoelasticity requires an optically birefringent object (specimen). Moiré interferometry, on the other hand, which produces massive amounts of data, is sensitive to rigid body rotations (unlike the CGS interferometer in question). Some of these limitations are overcome in the CGS method. It is a full-field optical technique applicable to both transparent and opaque materials, and does not require optical birefringence. In addition it provides an easily variable sensitivity (angular resolution of rays). The method's ability to produce fringes in real time, in conjunction with its relatively small light intensity loss, makes it a suitable candidate for mapping dynamic crack tip fields, where exposure times of the order of nanoseconds are required. Such a full field method is necessary in dynamic experiments in order to accurately measure dynamic stress intensity factors and establish regions of K-dominance. (A K-dominant region is defined as one in which the in-plane stresses are well approximated by the first (and singular) term of a Williams type expansion, see Tippur et al.[13])

The method of CGS for use in mechanics was first proposed by Tippur et al.[14] The setup of the method in a transmission configuration is shown in Figure 1. A coherent, monochromatic, collimated laser beam is incident on a deformed specimen. After transmission through
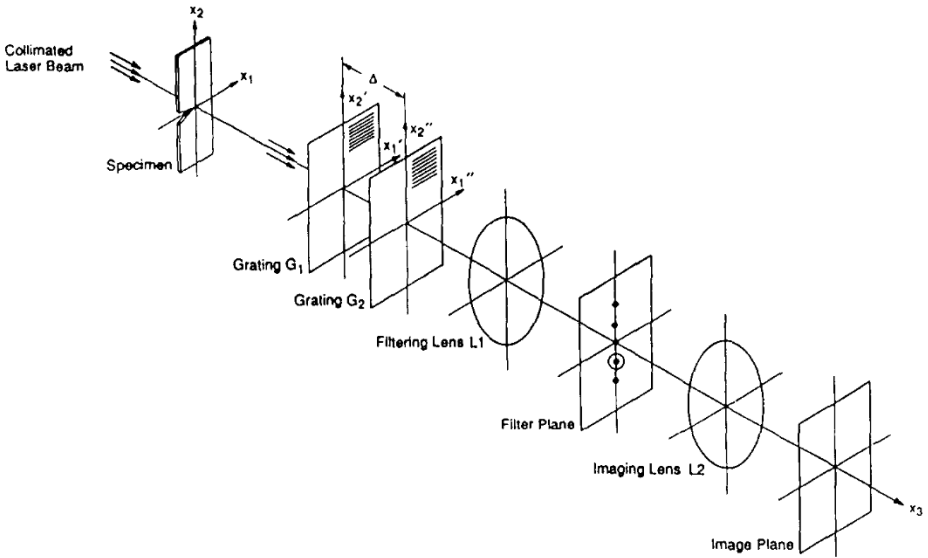
Fig. 1. Schematic of the setup for CGS in transmission.

the specimen it acquires an optical path difference and loses collimation. The resulting, now non-collimated, beam passes through two line diffraction gratings of fine pitch p. They are situated a distance Δ apart and perform a shearing of the incident wave front. The gratings' output intensity is transmitted through a filtering lens to obtain a diffraction spot pattern on the filtering plane, which is located at the focal plane of the lens. All but the first diffraction orders are blocked at this plane. The one remaining diffraction spot is imaged to produce an interference pattern.

In the analysis of Ref. 14 the technique was investigated using geometrical optics. In the present paper we provide a thorough analysis of the CGS technique, based on Fourier wave optics. The Fraunhofer far-field approximation is used to linearize the integrand in the Kirchhoff integral representation of the electromagnetic field resulting from the diffraction gratings. In addition, the paraxial approximation is used to obtain the light intensity distribution from the filtering lens. The current approach provides accurate far-field results that can be confidently used under far-field conditions that are valid for our experiment. Note that the final conditions for interference are the same as those obtained in Refs 13 and 14 even though the approach is different. Note also that Tippur[15] has recently produced a Fourier optics analysis of the CGS method using the Fresnel approximation. This analysis is rather complicated and uses near-field approximations. In the present paper

we show that the much simpler Fraunhofer far-field approximation can be used for all components in the optical setup by employing the simple device described in Section 2 that circumvents the need for direct calculation of the electromagnetic field at each station. In addition, in the present paper, unlike in the work of Ref. 15, the effects of large beam shearing are investigated.

At this point it should be noted that much of the first part of Section 2 (immediately following) deals with very basic issues of the theory of Fourier optics. Researchers with a significant amount of experience in this field will find most of it well known. It is suggested that such readers proceed to Section 3. However, for the benefit of researchers in the mechanics community who are not as familiar with these concepts, we have presented them here so that sufficient background material for complete understanding of our analysis procedure is presented. Readers unfamiliar with the details of Fourier optics theory need not refer to more specific publications.

2 FOURIER ANALYSIS OF CGS

An analysis of the optical method can be performed using either geometric or Fourier optics, depending upon the situation of interest. However, many occasions necessitate the use of wave optics. Components such as diffraction gratings cannot be adequately treated using geometrical optics. Such cases warrant the use of a more sophisticated treatment. Indeed, the most crucial role in the CGS system is played by the two diffraction gratings (see Fig. 1). These introduce double diffraction in the distorted light beam, which is what actually carries the information that we wish to extract about the deformation.

The far-field diffraction of a light wave at a grating can be modeled by adopting the Fraunhofer diffraction theory. Consider such a wave incident on a fine diffraction grating of square wave transmittance. This wave will be diffracted into an infinite number of wavefronts. Each diffracted beam (normal to a wavefront) can be labeled by an integer of order n, as shown in Fig. 2. The magnitude of the electromagnetic field of each diffracted beam is the corresponding Fourier coefficient of the transmission function of the grating. In the subsequent discussion we will look into the details of the Fourier analysis for the gratings and the filtering lens. In step 1 we consider the effect of diffraction of a distorted beam by one diffraction grating. The second step uses the results of step 1 to obtain the combined effects of both gratings. In step 3 the lens and spatial filtering at the aperture plane is analyzed. Finally
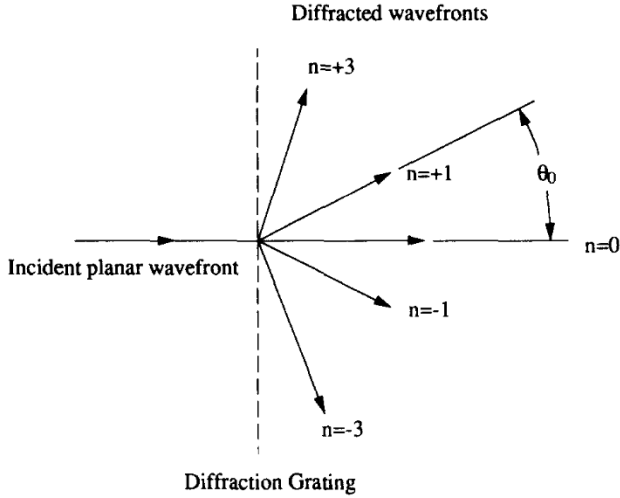
Diffracted wavefronts

Fig. 2. Diffracted wavefronts at a square transmittance diffraction grating.

in step 4 the light intensity distribution on the image is determined and the condition for constructive interference (bright fringes) is extracted.

In this paper we have chosen to present some details of the diffraction analysis that may be considered fundamental to researchers in the field of optics. However, since it is our intention to also expose researchers in mechanics to this new optical method, we feel that we should present enough background material so that all the details and assumptions of the analysis can be comprehended.

Step 1: Diffraction and gratings

Consider a transparent specimen, situated at the object plane, and assumed to be initially stress free and of uniform thickness. A collimated and coherent beam is transmitted through the specimen. As the specimen deforms, because of externally applied loads, the electromagnetic light field exiting the specimen is disturbed. The resulting beam is no longer collimated. The electromagnetic field E_0 formed just after the deformed specimen can be written as

$$E_0(x_1, x_2) = A_0 e^{ikS(x_1,x_2)} \tag{1}$$

where x_1 and x_2 are coordinates on the specimen, A_0 is the complex amplitude coefficient of the incident light wave, k is the wave number of the incident light wave and S is an optical path difference introduced in the beam by the deformation of the specimen (see Section 3.1). The
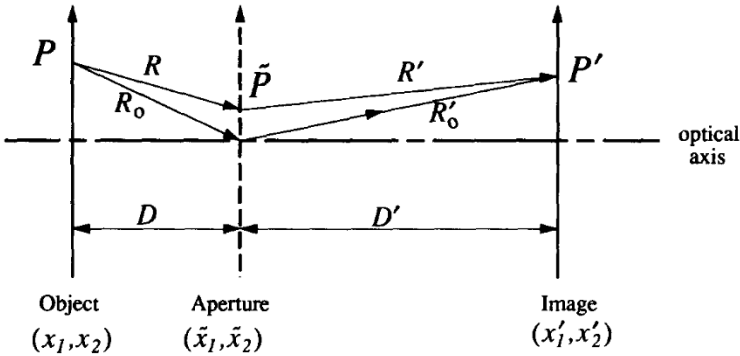
Fig. 3. Mapping of a point source from object to image planes from a generalized aperture.

optical path change S introduced implies that rays emerging from the specimen now deviate from parallelism. Note that eqn (1) can also be the result of the wavefront reflected from an opaque specimen (see Section 3.2).

Consider now such an electromagnetic field E_0 incident onto an aperture device, as shown schematically in two dimensions in Fig. 3. The aperture can be anything that causes diffraction (e.g. grating or aperture hole). A point source $P(x_1, x_2)$ on the object plane is imaged onto a point $P'(x_1', x_2')$ on the image plane. With reference to Fig. 3 it can be seen that x_1, x_2 and x_1', x_2' are the spatial coordinates in the object and image planes, respectively. We can define a transfer function h' between points P and P'. The resultant electromagnetic field, E', on the image plane can then be obtained by integrating the transfer function h' and the field, E_0, on the object plane. This is given by:

$$E'(x_1', x_2') = \int_{A_0} h'(x_1', x_2'; x_1, x_2) E_0(x_1, x_2) \, \mathrm{d}A_x \qquad (2)$$

where A_0 is the area of the incident wavefront. Note that eqn (2) is a general result. In our particular case E_0 will be given by eqn (1).

A general form of the transfer function h' of an aperture operator is given by Ref. 16.

$$h'(x_1', x_2'; x_1, x_2) = A \int_{\tilde{A}} \tilde{\tau}(\tilde{x}_1, \tilde{x}_2) \frac{\mathrm{e}^{-ik(R+R')}}{RR'} \, \mathrm{d}A_{\tilde{x}} \qquad (3)$$

In this expression $\tilde{\tau}$ is the transmission function for the aperture plane, $\tilde{A}$ is the region on the aperture plane that is open, i.e. allows light to pass through, and $\tilde{x}_1$ and $\tilde{x}_2$ are the spatial coordinates on the aperture

plane. The propagation distances R and R' are defined by

$$R = \sqrt{(\tilde{x}_1 - x_1)^2 + (\tilde{x}_2 - x_2)^2 + D^2}$$
$$R' = \sqrt{(\tilde{x}_1 - x_1')^2 + (\tilde{x}_2 - x_2')^2 + D'^2}$$

(4)

where D is the distance between object and aperture planes and D' is that between aperture and image planes (see Fig. 3). If in eqn (4) we set $\tilde{x}_1 = 0$ and $\tilde{x}_2 = 0$, we obtain the distance of points P and P' from the origin of the aperture plane, i.e.

$$R_0 = \sqrt{x_1^2 + x_1^2 + D^2}$$
$$R_0' = \sqrt{x_1'^2 + x_2'^2 + D'^2}$$

(5)

Using the Fraunhofer approximation we can linearize the propagation distances R and R' in terms of $\tilde{x}_1$ and $\tilde{x}_2$, about R_0 and R_0', respectively. Such a linearization is valid in cases where R_0 and R_0' are much larger than the size of the aperture. The linearization is obtained by performing a Taylor series expansion of eqn (4) about R_0 and R_0' in terms of $\tilde{x}_1$ and $\tilde{x}_2$. This approximation is provided by

$$R \approx R_0 - \left(\frac{x_1}{R_0}\right)\tilde{x}_1 - \left(\frac{x_2}{R_0}\right)\tilde{x}_2$$

$$R' \approx R_0' - \left(\frac{x_1'}{R_0'}\right)\tilde{x}_1 - \left(\frac{x_2'}{R_0'}\right)\tilde{x}_2$$

(6)

In the above expressions the fact that $R_0^2 = D^2 + x_1^2 + x_2^2$ has been used. One can easily see that the conditions for the Fraunhofer diffraction theory to be a good approximation are that[2,16]

$$\max\left(|\tilde{x}_1|, |\tilde{x}_2|\right) \ll \min\left(\sqrt{R_0\lambda}, \sqrt{R_0'\lambda}\right)$$

(7)

where λ is the wavelength of the light used and is given by $k = 2\pi/\lambda$. To simplify the integrand in eqn (3) we can introduce another first-order approximation on the amplification factor $(RR')^{-1}$ as follows:

$$\frac{1}{RR'} \approx \frac{1}{R_0 R_0'}$$

(8)

This approximation does not cause any problems, since it is less sensitive to small changes. We can also make the following change of variables in eqn (3):

$$u = -\left(\frac{x_1}{R_0} + \frac{x_1'}{R_0'}\right)\Big/\lambda$$

$$v = -\left(\frac{x_2}{R_0} + \frac{x_2'}{R_0'}\right)\Big/\lambda$$

(9)

Variables u and v are called the spatial frequencies. Substituting the linearizations of eqns (6) and (8) and performing the change of variables of eqn (9) into the expression for the transfer function (3), we obtain:

$$h'(x_1', x_2'; x_1, x_2) = A \frac{e^{-ik(R_0 + R_0')}}{R_0 R_0'} T(u, v) \tag{10}$$

as the transfer function of an aperture under the Fraunhofer approximation. In the above $T(u, v)$ has essentially become the Fourier transform of the aperture transmission function $\tilde{\tau}(\tilde{x}_1, \tilde{x}_2)$ and is given by:

$$T(u, v) = \int_{-\infty}^{\infty} \tilde{\tau}(\tilde{x}_1, \tilde{x}_2) e^{-i2\pi(u\tilde{x}_1 + v\tilde{x}_2)} \, dA_{\tilde{x}} \tag{11}$$

As was mentioned earlier, the function $\tilde{\tau}(\tilde{x}_1, \tilde{x}_2)$ on the aperture plane can be the transmission function of any diffracting instrument. The particular gratings used in our experiments have a square profile, as shown in Fig. 4. They consist of alternating lines of transparent and opaque regions of the same width. For an infinite grating, the transmission function can be written as a Fourier series, since it is periodic. This is:

$$\tilde{\tau}(\tilde{x}_1, \tilde{x}_2) = \sum_{m=-\infty}^{\infty} T_m e^{i2\pi m\tilde{x}_1/p} \tag{12}$$

Here p is the pitch of the grating and T_m are the related Fourier coefficients, given by

$$T_m = \frac{1}{p} \int_{-p/2}^{p/2} \tilde{\tau}(\tilde{x}_1, \tilde{x}_2) e^{-i2\pi m\tilde{x}_1/p} \, d\tilde{x}_1, \qquad m = 0, \pm 1, \pm 2 \ldots \tag{13}$$

For simplicity, diffraction gratings are usually assumed to be sinusoidal in transmittance (as was the case in Ref. 14). The gratings in our experiments, though, closely approximate a square transmission function. In this case the Fourier coefficients become:

$$T_0 = \frac{1}{2}$$

$$T_m = 0 \qquad \text{when } m = \text{even} \tag{14}$$

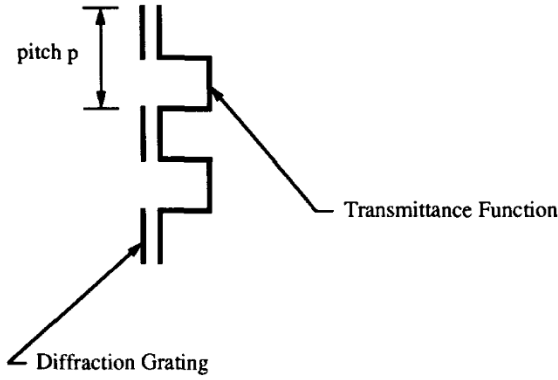$$T_m = \frac{(-1)^{(|m|-1)/2}}{\pi |m|} \qquad \text{when } m = \text{odd}$$

Fig. 4. Transmittance function of square transmittance diffraction grating.

We can use this Fourier series to compute the *Fourier transform* of the square grating in terms of the spatial frequencies, u and v, from eqn (11). This is given by:

$$T(u, v) = \sum_{m=-\infty}^{\infty} T_m \delta\left(u - \frac{m}{p}\right)\delta(v) \tag{15}$$

By substituting the above relationship into eqn (10) we can obtain the transfer function $h_G(u, v)$ for one square transmittance diffraction grating situated at the aperture plane. h_G is the transfer function from point source P to an image point P' though the grating of pitch p,

$$h_G(u, v) = \frac{Ae^{-ik(R_0+R_0')}}{R_0 R_0'} \sum_{m=-\infty}^{\infty} T_m \delta\left(u - \frac{m}{p}\right)\delta(v) \tag{16}$$

Here m is the diffraction order. It is clear that a square transmittance grating will cause an infinite number of diffracted wavefronts. These wavefronts have decreasing intensity since T_m is inversely proportional to m (as can be seen in eqn (14)).

We now have all the necessary tools to derive the electromagnetic field distribution E' on the image plane, resulting from the passage of E_0 through a diffraction grating. We can substitute eqn (16) into eqn (2) and perform the relevant integration to obtain E'. Alternatively, the resultant effects of the grating can be viewed as the image of a *modified* object with an electromagnetic field $E_0^{(1)}$, which produces exactly the same image E', but *without* the grating, i.e. by translation. This means that if the grating were removed then the electromagnetic field at the object plane would have to become $E_0^{(1)}$ in order to maintain the same field E' at the image plane, with the Fraunhofer condition being satisfied. We prefer this approach because it facilitates the easy inclusion of the effects of the second grating as seen in step 2. It is simple to show that the modified field $E_0^{(1)}$ can be expressed as the summation of many spatially displaced E_0's as follows:

$$E_0^{(1)}(x_1, x_2) = A \sum_{m=-\infty}^{\infty} T_m E_0(x_1 + mR_0\theta_0, x_2) \qquad (17)$$

where θ_0 is the grating diffraction angle given by

$$\theta_0 = \sin^{-1}\frac{\lambda}{p} \approx \frac{\lambda}{p} \qquad (18)$$

Note that the grating produces many virtual images at angles of integer multiples of θ_0. Also note that a virtual image corresponding to the amplitude $A T_m$ has been shifted in the x_1 direction by an amount $mR_0\theta_0$ from the original position on the object.

Step 2: Virtual image of double gratings

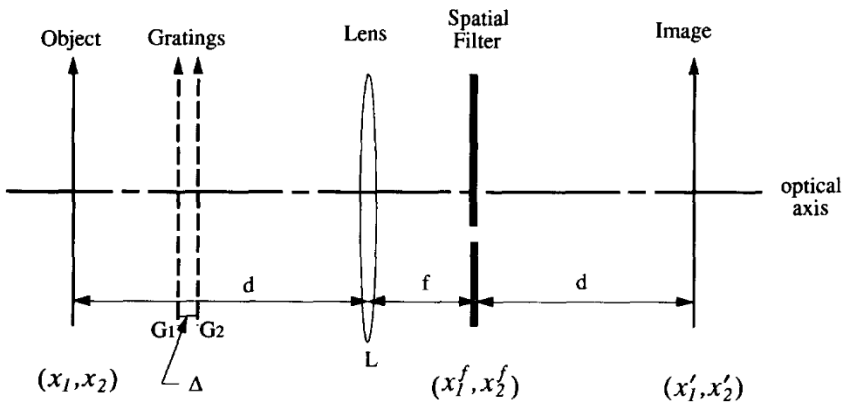A side view of the CGS setup is shown in Fig. 5, along with the

Fig. 5. Profile of the CGS setup.

associated coordinate systems on each plane. The effect of gratings G_1 and G_2 on E_0 can be obtained from the results in step 1. If the first grating is removed it will produce a set of virtual images having an equivalent electromagnetic distribution given by eqn (17) in order to maintain an electromagnetic distribution E' at the object plane. This will act as an object distribution for the second grating G_2. Note that we can use the Fraunhofer approximation for the second grating as well, because we have found an effective image plane distribution (caused by the removal of the first grating), but which has been translated to the far-field. The second grating will now also produce an infinity of virtual images for each virtual image generated by the first grating, by following exactly the same operation as in (17) but acting on $E_0^{(1)}$. Thus the idea is to undergo a procedure in which each grating is sequentially removed and the far-field object distribution on the (x_1, x_2) plane is modified in a way so as to always keep the field E' on the image plane the same. A schematic of the equivalence of object electromagnetic distribution, at the far field, for the removal of the two gratings is shown in Fig. 6. We see that first G_1 is removed and E_0 is modified to $E_0^{(1)}$, at the far field, given by eqn (17). Then the second grating is removed to obtain an equivalent object distribution $E_0^{(2)}$. $E_0^{(2)}$ is easily constructed by repeating the operation of eqn (17), but with $E_0^{(1)}$ replacing the electromagnetic field inside the summation, i.e.

$$E_0^{(2)} = \sum_{m=-\infty}^{\infty} \sum_{l=-\infty}^{\infty} T_m T_l E_0(x_1 + (m + l)R_0\theta_0 + m\Delta\theta_0, x_2) \qquad (19)$$

The whole procedure is such that E' on the image plane remains unchanged. From eqn (19) one can see that each virtual image corresponding to the amplitude $AT_m T_l$ is shifted in the x_1 direction by $(m + l)R_0\theta_0 + m\Delta\theta_0$, where Δ is the spacing between the gratings. Diffraction orders after the second grating are given by $m + l =$ constant in eqn (19).

In general it would seem that because of the double summation there would be many combinations of m's and l's resulting in the sum $m + l$ to equal the same constant. This would mean the superposition (and interference) of many wavefronts, making data reduction extremely difficult. The nature of the Fourier coefficients T_m (eqn (14)), though, produces a simple result for the orders $m + l = \pm 1$. Diffraction order $m + l = 1$, for example, will contain a superposition of wavefronts corresponding to the pairs $m = 0$, $l = 1$ and $l = 0$, $m = 1$ only, because for all other combinations resulting in $m + l = 1$ either T_m or T_l would
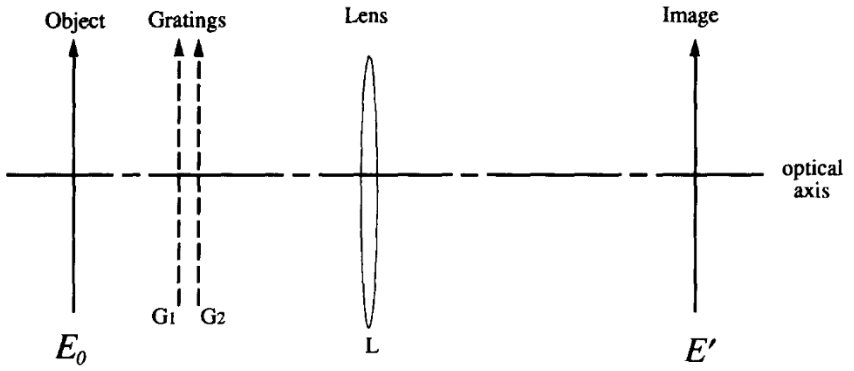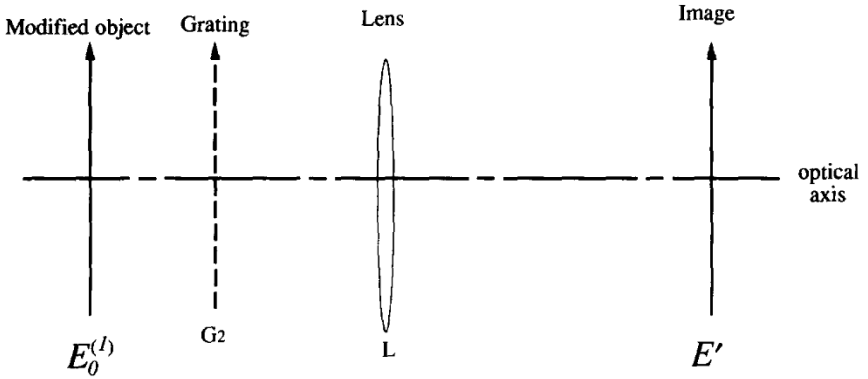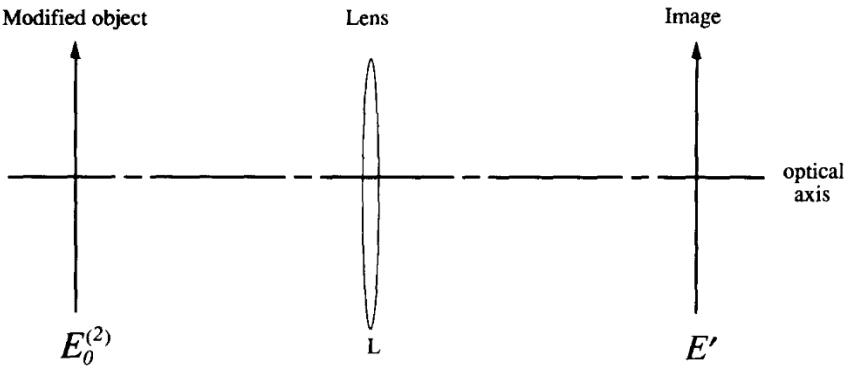
Fig. 6. Schematic illustration of the object transformation necessary to keep the image field distribution the same upon successive removal of the two CGS diffraction gratings.

be zero by virtue of eqn (14). Therefore, for the $m + l = 1$ order, $E_0^{(2)}$ becomes

$$E_0^{(2)}|_{1\text{st}} = T_0 T_1 E_0(x_1 + R_0 \theta_0, x_2) + T_1 T_0 E_0(x_1 + R_0 \theta_0 + \Delta\theta_0, x_2) \quad (20)$$

The first term is for $m = 0$, $l = 1$ and the second for $l = 0$, $m = 1$. At this point it is clear from eqn (20) that the $+1$ (or -1) diffraction order is the superposition of *only two* wavefronts sheared with respect to each other by an amount $\Delta\theta_0$ in the x_1 direction. Such a superposition will create interference fringes that can be easily analyzed. Looking at any other diffraction order $m + l = \text{constant}$ will involve superposition of many wavefronts.

Step 3: Lens and spatial filtering

A spatial filtering lens is necessary for the purpose of isolating a perceivable fringe pattern from the ± 1 diffraction orders. It is well known that the field distribution at the focal plane of a lens is related to the Fourier transform of the field on the object plane. Also, the electromagnetic field distribution on the image plane is related to the Fourier transform of the field on the focal plane. To simplify the analysis we assume an infinite lens. Using Abbe's theory[2] for an infinite lens and the Fraunhofer approximation, the formula of the local mapping from the object to the lens focal plane is given in Klein and Furtak[16] as follows:

$$E^f(x_1^f, x_2^f) = \frac{i}{\lambda f} e^{-ik(d+f)} e^{i(r^f)^2/2d'} \mathscr{F}\{E_0^{(2)}\}\left(\frac{-x_1^f}{\lambda f}, \frac{-x_2^f}{\lambda f}\right) \quad (21)$$

Here x_1^f and x_2^f are Cartesian coordinates on the focal plane, r^f is the radial coordinate, f the focal length of the lens, d the distance of the object from the lens and d' the distance of the image from the focal plane. $\mathscr{F}$ represents the Fourier transform operation. Note that larger spatial frequencies will appear on the focal plane further away from the optical axis.

The field distribution at the image plane can be represented in terms of the Fourier transform of the distribution at the focal plane as

$$E' = \frac{1}{\rho} e^{-ik(d+Z+r'^2/2d')} \int_A \mathscr{F}\{E_0^{(2)}\}(u^f, v^f) e^{i2\pi[u^f(x_1'/\rho) + v^f(x_2'/\rho)]} \, du^f \, dv^f \quad (22)$$

where the spatial frequencies u^f and v^f are defined as

$$u^f = \frac{x_1^f}{\lambda f}, \qquad v^f = \frac{x_2^f}{\lambda f} \quad (23)$$

In eqn (22) we have used $E_0^{(2)}$ as the object field for the lens L. You may recall that in our case $E_0^{(2)}$ is the electromagnetic distribution containing the effects of the two diffraction gratings given by eqn (19); 'ρ' is the transverse magnification defined by

$$\rho = -\frac{d'}{f} \qquad (24)$$

From the expression for $E_0^{(2)}$ (see eqns (19) and (1)) and from eqn (21) it can be seen that the virtual images of the two gratings are projected as distinct diffraction spots on the focal plane of the filtering lens. This is because the Fourier transform of sine and cosine functions (or complex exponentials as in eqn (1)) are delta functions. Filtering can now be performed at the lens focal plane simply by physically blocking all undesired diffraction spots. In the CGS setup all spots are blocked except for the $+1$ or -1 orders. These are the ones on either side of the central, brightest, diffraction spot.

   Although it is very simple to block all but the desired orders, we can also obtain a mathematical representation of the filtering process. To obtain the final, filtered, distribution E' on the image plane, we substitute for $E_0^{(2)}$ in eqn (22) from eqn (19), but now the integration in eqn (22) is performed over some spatial limits on the lens focal plane.

$$E'(x_1', x_2') = \frac{1}{m} e^{-ik(d+Z+r'^2/2d')}$$

$$\times \int_{\omega_0 - \delta\omega_0}^{\omega_0 + \delta\omega_0} \mathscr{F}\left\{ \sum_{m=-\infty}^{\infty} \sum_{l=-\infty}^{\infty} T_m T_l E_0(x_1 + (m+l)R_0\theta_0 + l\Delta\theta_0, x_2) \right\}(u, v)$$

$$\times e^{i2\pi[u(x_1'/\rho) + v(x_2'/\rho)]} \, du \, dv \qquad (25)$$

The filtering occurs by the limits on the integral sign. It is clear that the filter on the focal plane is isolating wavefronts whose Fourier components are in the range $\omega_0 - \delta\omega_0 < u < \omega_0 + \delta\omega_0$. If the deflection angles introduced by the specimen deformation are smaller than the diffraction angle induced by the square gratings, then all the information about the deformation in the specimen is obtained by the light passing through the mth order point on the focal plane of the lens. This means that there is no crosstalk between diffraction spots formed on the focal plane.

   The only order that survives after filtering is that for $m = 1$. Equations (20) and (14) then give

$$E_0^{(2)}|_{1st} = \frac{1}{2\pi} (E_0(x_1 + R_0\theta_0, x_2) + E_0(x_1 + R_0\theta_0 - \Delta\theta_0, x_2)) \qquad (26)$$

As was mentioned earlier, only this order contains two interfering wavefronts. The image of the field of eqn (26) is $E'_{1st}(x'_1, x'_2)$ and is given through eqn (25) by

$$E'|_{1st}(x'_1, x'_2) = \frac{A}{2\pi} \frac{1}{\rho} e^{-ik(d + Z + r'^2/2X')} \times \left(e^{ikS((x'_1 + R_0\theta_0)/\rho, x'_2/\rho)} + e^{ikS((x'_1 + R_0\theta_0 - \Delta\theta_0)/\rho, x'_2/\rho)} \right)$$

(27)

In the above expression we have made use of eqns (26) and (1). The information about the deformation is contained in this electromagnetic light field distribution.

Step 4: Light intensity and fringe pattern on the image plane

The light intensity I' on the image plane is obtained from the relation

$$I'(x'_1, x'_2) = E' * \bar{E}'$$

(28)

where $\bar{E}'$ is the complex conjugate of the electromagnetic field E'. Using eqn (27), I' can easily be calculated as

$$I' = 2\left(\frac{A}{2\pi}\frac{1}{\rho}\right)^2 \{1 + \cos\left[k(S((x'_1 + R_0\theta_0)/\rho, x'_2/\rho)\right.$$
$$\left. - S((x'_1 + R_0\theta_0 - \Delta\theta_0)/\rho, x'_2/\rho))\right]\}$$

(29)

The local maxima of light intensity will appear as bright interference fringes on the image plane. The condition for constructive interference is

$$k(S((x'_1 + R_0\theta_0)/\rho, x'_2/\rho) - S((x'_1 + R_0\theta_0 - \Delta\theta_0)/\rho, x'_2/\rho)) = 2n\pi,$$
$$n = 0, \pm 1, \pm 2, \ldots \quad (30)$$

i.e. the cosine has its maximum value of 1. Using $k = 2\pi/\lambda$ the interference relationship becomes

$$\langle S \rangle_\delta = n\lambda$$

(31)

Here, n is an integer fringe order, δ is the image shearing distance and $\langle S \rangle_\delta$ denotes the optical path change between the sheared and unsheared images. The shearing distance, δ, is given by,

$$\delta \approx \frac{\Delta\theta_0}{\rho} \approx \Delta \frac{\lambda}{\rho p}$$

(32)

In the above we have made use of eqn (18) and the image magnification ρ on the image plane is still included. Note that we can derive the

relationship of eqn (31) to the interference condition with a simple calculation, as is shown in Mason *et al.*[17] If the image shearing is small enough, we can approximate the difference operation in equation (31) by a differential form of the optical path, so that

$$\frac{\partial S(x_1, x_2)}{\partial x_1} = \frac{np}{\Delta}, \qquad n = 0, \pm1, \pm2, \ldots \qquad (33)$$

In eqn (33) we have expressed S as a function of (x_1, x_2), i.e. on the object plane. That is why the magnification factor has been removed. Equation (33) is the fundamental relationship for fringe creation in the method of CGS. It relates the gradient of the optical path change introduced in the collimated beam to the fringe order n on the image plane. One can go through a similar process, but with the gratings' lines set perpendicular to the x_2 direction to obtain shearing in the x_2 direction. Then we obtain

$$\frac{\partial S(x_1, x_2)}{\partial x_2} = \frac{mp}{\Delta}, \qquad m = 0, \pm1, \pm2, \ldots \qquad (34)$$

Up to this point the analysis is equally applicable to a transmission or reflection setup. The difference between the two methods will be in interpreting the effects of deformation on S.

Note that the approach in Ref. 14, 15 does not allow the use of the method when a large grating separation exists, since the analysis presented there directly results in the approximate relations (33) and (34). The current work justifies the interpretation of CGS fringes as differences of optical path change, as seen in eqn (30). Conditions under which relation (30) can be reduced to (33) or (34) have been examined in Bruck and Rosakis.[18,19]

3 APPLICATIONS OF CGS

The application of CGS to fracture mechanics was described in Ref. 8. However, the technique can be used for the study of a variety of solid mechanics problems. In this section we shall show the applicability of the method to both transmission and reflection setups and provide some examples of the method's results.

3.1 Relationship between specimen deformation and optical path change S in transmission

Consider a collimated coherent monochromatic light beam incident normally onto an optically isotropic, transparent specimen of uniform

nominal thickness h and refractive index n_0. Deformation of the plate specimen will introduce an optical path change $S(x_1, x_2)$ in the transmitted wavefront. This is given by the elasto-optical equation (Rosakis and Ravi-Chandar[20]):

$$S(x_1, x_2) = 2h(n_0 - 1) \int_0^{1/2} \varepsilon_{33} \, dx_3/h + 2h \int_0^{1/2} \delta n \, dx_3/h \qquad (35)$$

where ε_{33} is the strain component through the thickness of the plate and δn is the change in the refractive index through the specimen. The first integral in eqn (35) represents the net optical path difference because of changes in plate thickness caused by strain. The second term is the result of changes in material refractive index because of stress present in the specimen. For an optically and mechanically isotropic linear elastic solid this change, δn, depends upon the stress state though the Maxwell relation (Born and Wolf[2]):

$$\delta n(x_1, x_2, x_3) = D_1(\sigma_{11} + \sigma_{22} + \sigma_{33}) \qquad (36)$$

where D_1 is the stress-optic constant and σ_{ij} are the Cartesian components of the Cauchy stress tensor induced by the deformation. We can use the same assumptions to relate the strain component ε_{33} to the stress state from the linear elastic constitutive law. Substituting this result and eqn (36) into eqn (35) we get

$$S(x_1, x_2) = 2c_\sigma h \int_0^{1/2} \left\{ (\sigma_{11} + \sigma_{22}) \left(1 + D_2 \left[\frac{\sigma_{33}}{v(\sigma_{11} + \sigma_{22})} \right] \right) \right\} dx_3/h \qquad (37)$$

where $c_\sigma = D_1 - v(n_0 - 1)/E$, E and v are the Young's modulus and Poisson's ratio of the material, respectively, and D_2 is a modified optical constant given by:

$$D_2 = \frac{vD_1 + v(n_0 - 1)/E}{D_1 - v(n_0 - 1)/E} \qquad (38)$$

In eqn (37) the term in the square brackets, $\sigma_{33}/v(\sigma_{11} + \sigma_{22})$, illustrates the degree of plane strain. If it is $+1$, a plane-strain two-dimensional approximation is appropriate. When plane stress is a good approximation to the three-dimensional situation (for example in very thin experimental specimens) then eqn (37) reduces to

$$S(x_1, x_2) \approx c_\sigma h(\hat{\sigma}_{11} + \hat{\sigma}_{22}) \qquad (39)$$

where $\hat{\sigma}_{11}$ and $\hat{\sigma}_{22}$ are the thickness averages of σ_{11} and σ_{22},

respectively. Substituting eqn (39) into eqn (33), we obtain the CGS relations for transmission under plane stress conditions:

$$\frac{\partial(\hat{\sigma}_{11} + \hat{\sigma}_{22})}{\partial x_1} = \frac{np}{c_\sigma h \Delta}, \qquad n = 0, \pm1, \pm2 \cdots \qquad (40)$$

3.2 Relationship between specimen deformation and optical path change S in reflection

In this section we shall provide an analysis similar to that above, but for the case of reflection. Consider a specimen whose reflective and initially flat surface occupies the (x_1, x_2) plane. After deformation the specimen surface will no longer be flat. The new surface will be described by a function $F(x_1, x_2, x_3)$.

$$F(x_1, x_2, x_3) = x_3 + u_3(x_1, x_2) = 0 \qquad (41)$$

where u_3 is the out-of-plane displacement component on the specimen surface. Now the change in the optical path difference depends only upon ε_{33} as follows:

$$S(x_1, x_2) = 2u_3(x_1, x_2, h/2) = 2h \int_0^{1/2} \varepsilon_{33}(x_1, x_2, x_3)\, dx/h \qquad (42)$$

To this point we have not assumed any constitutive behavior, but we have used a small strain approximation. Specializing eqn (42) to a linearly elastic and isotropic solid we get

$$
\begin{aligned}
S(x_1, x_2) &= 2u_3(x_1, x_2, h/2) \\
&= -\frac{2vh}{E} \int_0^{1/2} \left\{ (\sigma_{11} + \sigma_{22}) \left[1 - \frac{\sigma_{33}}{v(\sigma_{11} + \sigma_{22})} \right] \right\} dx_3/h \qquad (43)
\end{aligned}
$$

Utilizing a plane stress approximation as before,

$$S(x_1, x_2) = 2u_3(x_1, x_2, h/2) \approx -\frac{2vh}{E}(\hat{\sigma}_{11} + \hat{\sigma}_{22}) \qquad (44)$$

Substituting the above in eqn (33) we end up with

$$\frac{\partial u_3}{\partial x_1} = \frac{np}{2\Delta}, \qquad n = 0, \pm1, \pm2 \cdots$$

or   (45)

$$-\frac{vh}{E}\frac{\partial(\hat{\sigma}_{11} + \hat{\sigma}_{22})}{\partial x_1} = \frac{np}{2\Delta}, \qquad n = 0, \pm1, \pm2 \cdots \text{ for plane stress}$$

These equations describe the CGS fringes in a reflection setup and are analogous to eqn (40). Note that in this case the fringes represent contours of constant gradient of out-of-plane displacement on the specimen surface.

3.3 Static and dynamic experimental results

Static experiments
A typical interferogram generated by the CGS method is shown in Fig. 7(a). This is in a transmission setup on an edge-cracked PMMA plate loaded in a three-point bend configuration. This is a typical loading geometry used in fracture mechanics investigations, but the method can be used in many areas of experimental solid mechanics. In Fig. 7(b) we see the fringe pattern resulting from the application of a line load on an uncracked PMMA plate of large in-plane dimensions, thus approximating a line load on a half space. The stress field measured by CGS agrees well with that predicted from linear elasticity, over a large region of the body. In all these cases, which are in transmission, we can use equation (40) to evaluate the derivative of the in-plane stress components, *under plane stress conditions*. Therefore, in attempting to analyze a fringe pattern we must first establish the zone of two-dimensional plane stress conditions (if one exists) on the particular test specimen.

Let us consider in more detail the data reduction for one particular interferogram. Figure 8(a) shows an interferogram obtained from a statically loaded three-point bend specimen of a precracked bimaterial system, consisting of PMMA bonded to aluminum (from Lee and Rosakis[21]). Transmission CGS was used, hence we see only half the fringe pattern: the one on the PMMA side of the bond. Establishing the plane stress region of such a specimen can be done numerically using a three-dimensional calculation. For homogeneous specimens such a calculation was performed by Krishnaswamy *et al.*[22] For an interfacial specimen a similar analysis was made by Lee and Rosakis.[21] They show a three-dimensional zone extending ahead of the crack tip along the bond line. It has a width of approximately half a plate thickness. Figure 9 shows a three-dimensional contour plot of the quantity $\sigma_{33}/\nu(\sigma_{11} + \sigma_{12})$ (see eqns (37) and (43)), which is a measure of three-dimensionality. The dark region represents a value of zero, and corresponds to a two-dimensional situation in which eqns (40) and (45) are applicable. We can therefore collect a series of experimental points, from outside the three-dimensional region, which will give us the value of $\partial(\sigma_{11} + \sigma_{22})/\partial x_1$ at each location r_i, θ_i where r, θ are polar coordinates centered at the crack tip and i denotes the ith data point.
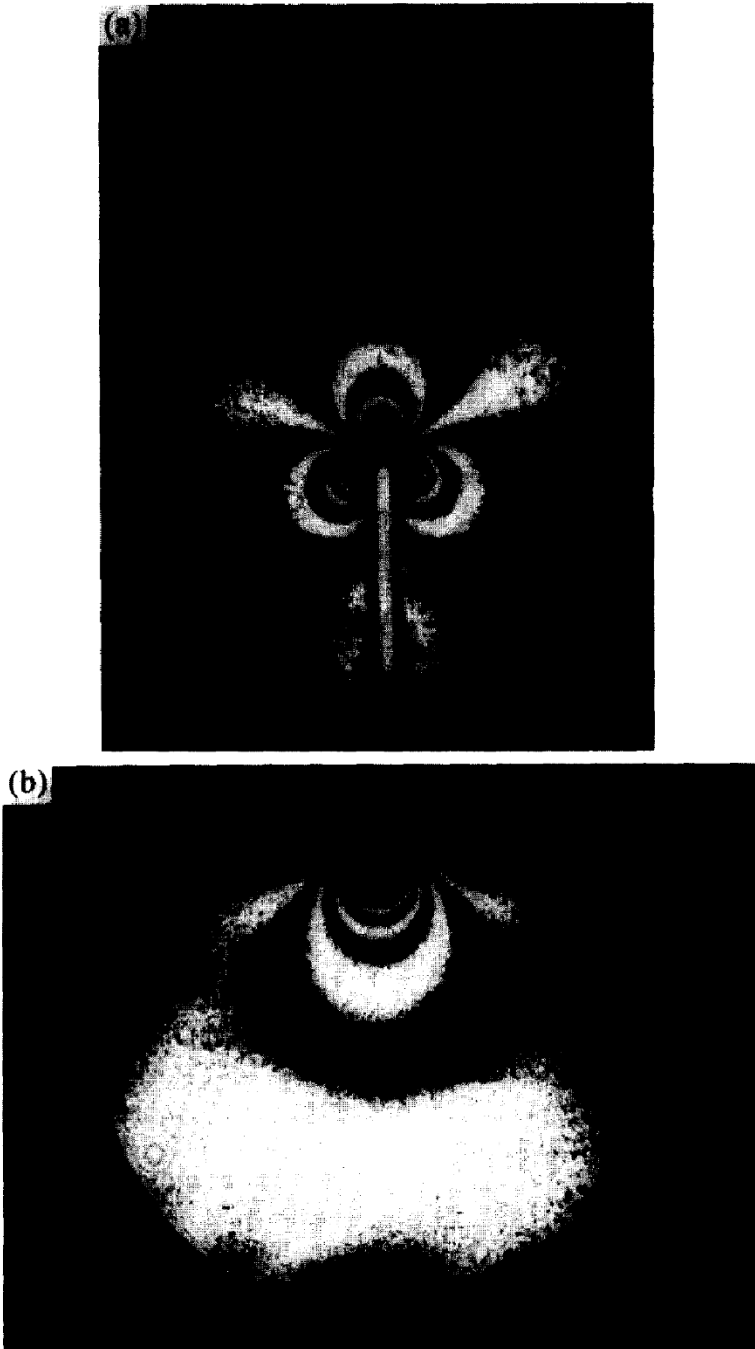
Fig. 7. Interferograms showing the CGS pattern around (a) the crack tip of an edge-notched plate under three-point bending and (b) the area of application of a line load to a large uncracked plate.
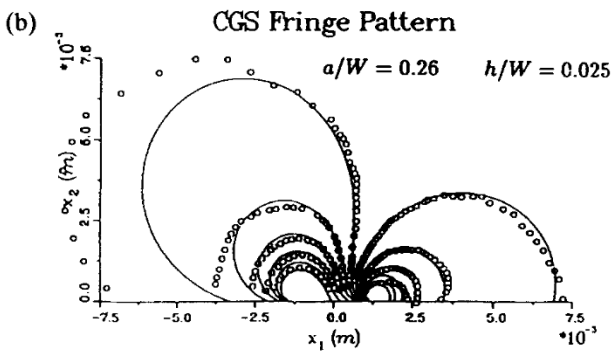
(a)

(b)   **CGS Fringe Pattern**

Fig. 8. (a) CGS interferogram at the crack tip of a PMMA/aluminum bimaterial subjected to three-point bending. (b) Superposition of experimental data points (from (a)) on solid lines generated by fitting a K-dominant stress field to the interferogram.

Asymptotic linear elasticity theory predicts the most singular in plane stress components around the crack tip as

$$\sigma_{ij} = \frac{1}{\sqrt{2\pi r}} [\text{Re } \{Kr^{i\varepsilon}\}\Sigma_{ij}^{I}(\theta, \varepsilon) + \text{Im } \{Kr^{i\varepsilon}\}\Sigma_{ij}^{II}(\theta, \varepsilon)] \qquad (46)$$

where $K = K_1 + iK_2 = |K|e^{i\psi}$ is the complex stress intensity factor as defined by Rice[23] for the in-plane modes, and Σ_{ij}^{I} and Σ_{ij}^{II} are the
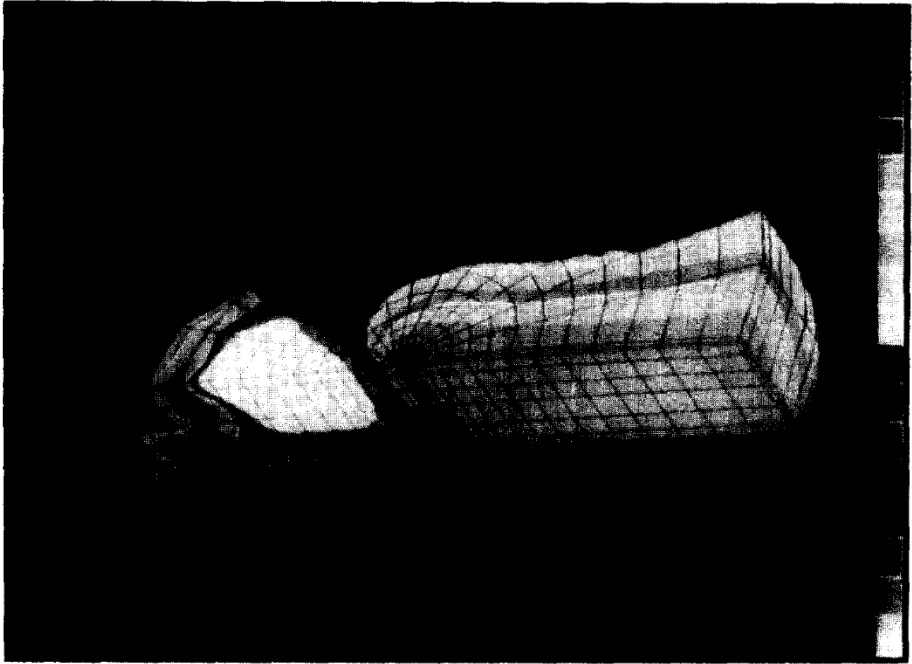
Fig. 9. Visualization of the region of three-dimensional deformation in a PMMA/aluminum edge-cracked plate subjected to three-point bending. Contours of constant $\sigma_{33}/\nu(\sigma_{11} + \sigma_{22})$ are shown. Only the PMMA side of the specimen is depicted. The top surface visible in the figure is the mid-plane of the specimen and the traction-free crack faces are on the left.

angular variations of stresses. The oscillatory index ε is material-dependent and characterizes the interface. It is given by

$$\varepsilon = \frac{1}{2\pi} \ln \left[\frac{\kappa_1 \mu_2 + \mu_1}{\kappa_2 \mu_1 + \mu_2} \right] \tag{47}$$

where $\kappa_\alpha = 3 - 4\nu_\alpha$ for plane strain and $(3 - \nu_\alpha)/(1 + \nu_\alpha)$ for plane stress, with μ_α, ν_α being the shear modulus and Poisson's ratio for each material ($\alpha = 1,2$). This is a two-dimensional field and is applicable for plane stress or plane strain conditions. The existence of such a field, though, must not be taken for granted if we manage to show that two-dimensional conditions apply. The two issues are completely different. So the existence of a field given by eqn (46), called a K-dominant field, in the specimen of Fig. 8(a) is something to be investigated.

Under the existence of a K-dominant field in a plane stress region, by combining eqns (46) and (40) we can get

$$\frac{\partial S(x_1, x_2)}{\partial x_1} = n\lambda$$

$$\approx c_\sigma h \frac{\partial(\hat{\sigma}_{11} + \hat{\sigma}_{22})}{\partial x_1}$$

$$= c_\sigma h \frac{\partial}{\partial x_1} \left\{ \frac{2e^{\varepsilon_\sigma(\theta - \pi)}}{\sqrt{2\pi r} \cosh(\pi\varepsilon_\sigma)} |K| \cos\left(\frac{\theta}{2} + \psi + \varepsilon_\sigma \ln r\right) \right\} \quad (48)$$

where n is the fringe order. In eqn (48) we have as unknowns the fracture parameters ψ and $|K|$. To extract these values from our experiment we can perform a least-squares fitting procedure on the collection of data points r_i, θ_i, n_i. After obtaining ψ and $|K|$ we can easily calculate K_1 and K_2. At this point we can check whether a K-dominant field does indeed exist in the particular specimen used (e.g. Fig. 8(a) in this case). It is possible to superimpose digitized data points from the actual fringe pattern to a set of CGS contours derived numerically using the fitted values of K_1 and K_2 as input. Such a composite is shown in Fig. 8(b). It is clear that the agreement is very good in regions of plane stress. This is as expected, since points inside the three-dimensional region cannot possible conform to a K-dominant field that is a two-dimensional field.

Dynamic experiments

Application of CGS to dynamic experiments is quite straightforward. The experimental setup is exactly the same as in the static case. The fringe pattern generated is imaged onto a high-speed camera, with a framing rate adequate for the particular experiments (typically 2×10^{-6}). A typical sequence of dynamic mixed-mode interferograms in transmission from a PMMA specimen impacted in a drop weight tower is shown in Fig. 10(a) and (b) (from Mason *et al.*[17]). The specimen and loading geometries are shown in the inset. A visible change in the fringe pattern in both size and rotation occurs over time. It can be easily shown that the lobe rotation is proportional to the mode mixity present in the field. The stress field seen in Fig. 10(a), (b) shifts from primarily mode II to a mode I field after about $300 \, \mu s$. It is possible to analyze each one of these interferograms using a procedure like that described
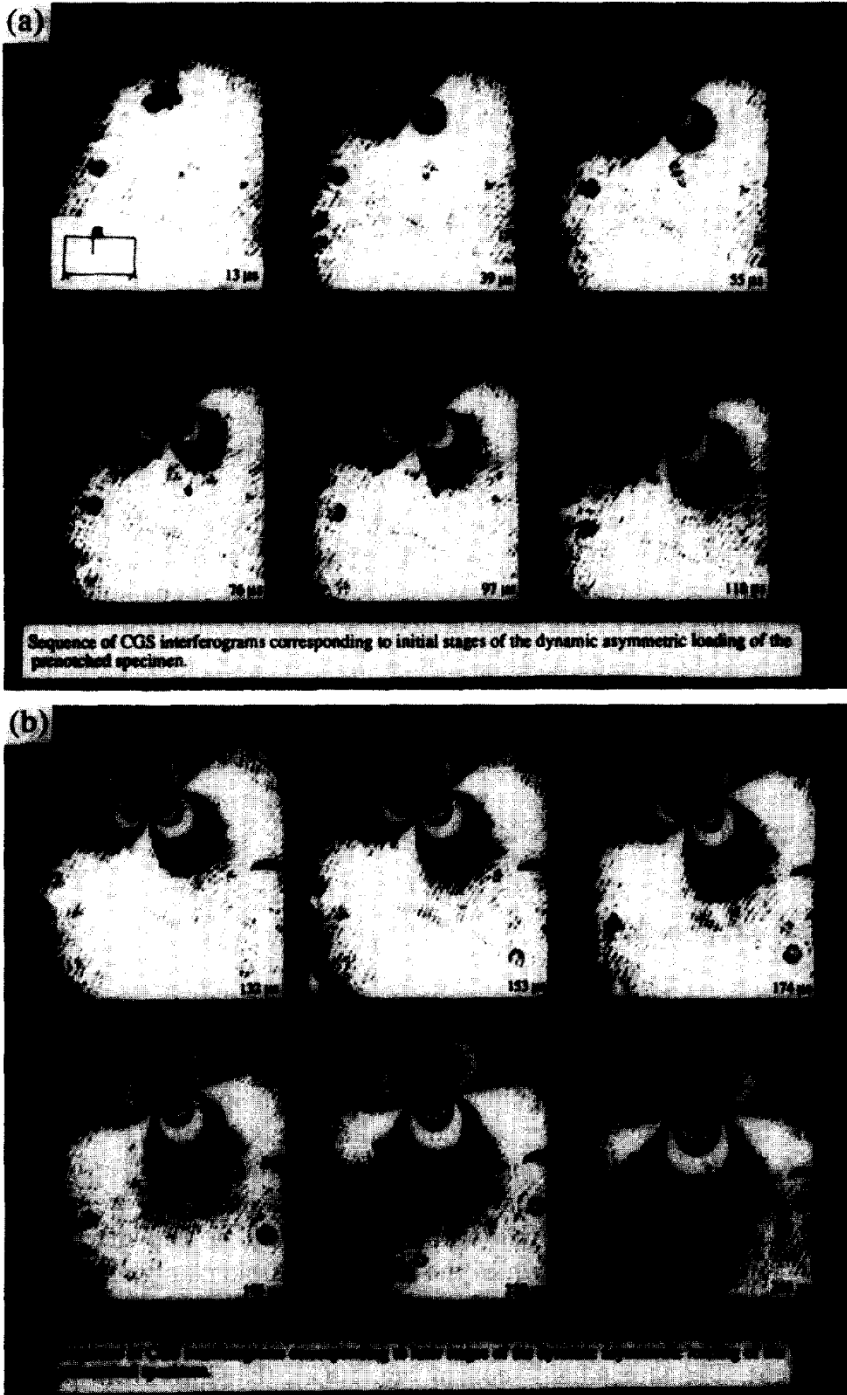
Fig. 10. Dynamic interferograms of an asymmetrically loaded edge-cracked PMMA plate (a) at short times after impact and (b) at long times after impact.

above. In a K-dominant situation, the in-plane stress field for a dynamically loaded stationary crack will be given by

$$\sigma_{\alpha\beta} = \frac{K_{\mathrm{I}}(t)}{\sqrt{2\pi r}} f^{\mathrm{I}}_{\alpha\beta}(\theta) + \frac{K_{\mathrm{II}}(t)}{\sqrt{2\pi r}} f^{\mathrm{II}}_{\alpha\beta}(\theta) \tag{49}$$

Here r and θ are plane polar coordinates centered at the crack tip, t is the time variable and Greek indices α and β have the range $1, 2$. Using eqns (49) and (40) we can perform a least-squares fit for K_{I} and K_{II} at each time, thus obtaining a time history of the fracture parameters.

The method of CGS has been applied in many other dynamic experiments. A study of dynamic K-dominance in three-point bend specimens was made in Ref. 24. Experiments and analysis of bimaterial specimens was performed in Ref. 25 and Refs 26–28. Also CGS imaging of dynamically deforming composite laminates has been performed in Ref. 29. A typical sequence of CGS interferograms resulting for the out-of-plane impact of a graphite/epoxy composite laminate is shown in Fig. 11. Since these experiments were performed in reflection, the observed fringe patterns represent contours of constant out-of-plane displacement gradient. By digitizing each fringe and performing a numerical integration of the displacement gradient, it is possible to derive the out-of-plane displacement history of the deforming laminate.

General applications

It is clear that the CGS method will produce a fringe pattern from any object that introduces an phase shift in the incident laser beam. For example, a fringe pattern may be obtained by passage of the beam through a gas or liquid with density variations. Density variations cause a change in refractive index. This means that the method may be used in fluid mechanics applications as well. Actually, it is very similar to Schlirien methods already used by fluid mechanicians. An example of the diverse abilities of the method is shown in Fig. 12. This is an interferogram produced by the passage of a laser beam through the flame plume of a Bunsen burner. Temperatures in the burner reach 1000 °C. This causes density variations which we see as fringes.

4 CONCLUSIONS

In this paper we present a simple and accurate analysis of CGS using Fourier wave optics. It has been demonstrated that by employing the procedure shown in Section 2 it is possible to use the Fraunhofer
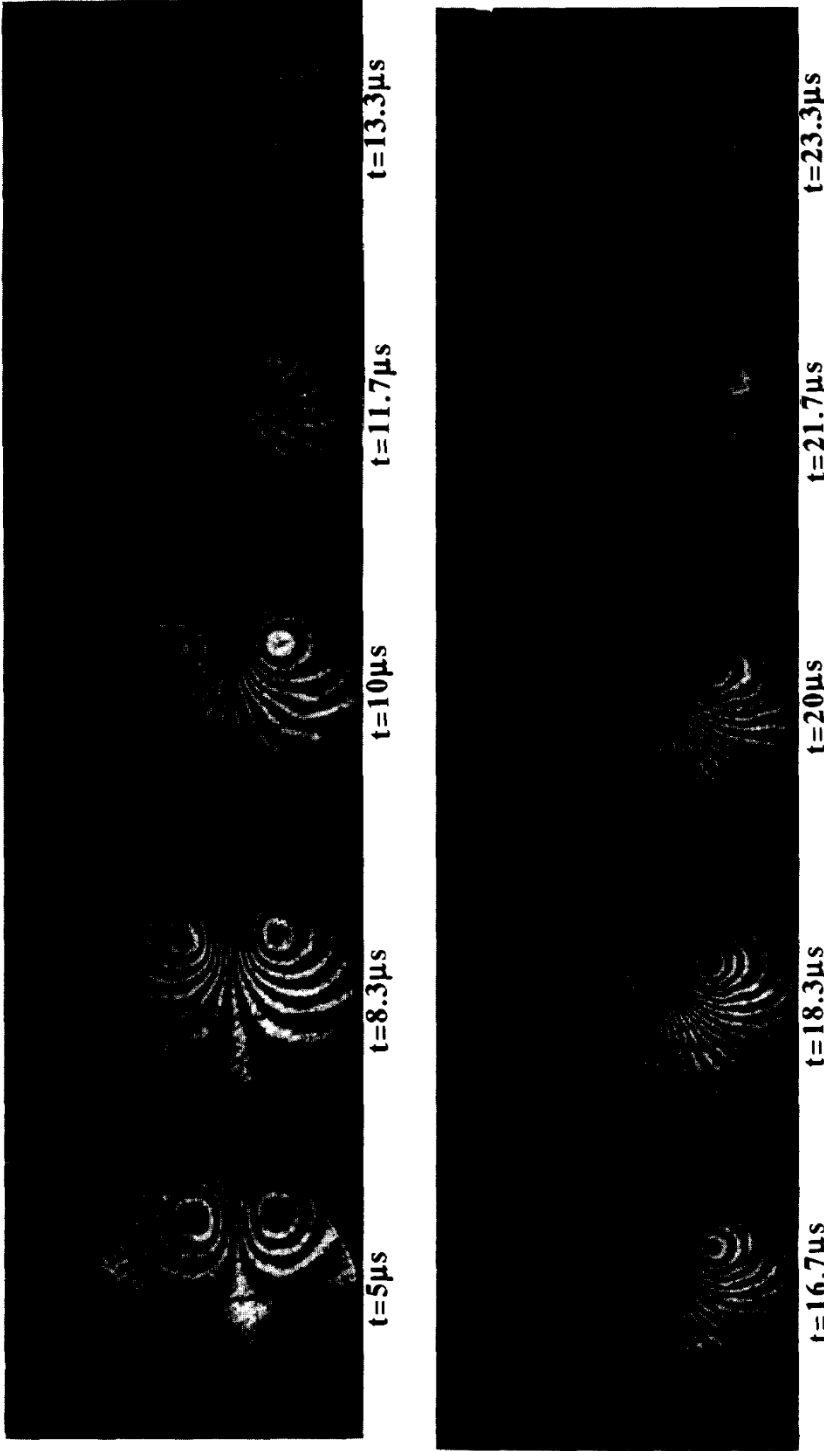
Yeong Joo Lee, John Lambros, Ares J. Rosakis

Fig. 11. Sequence of CGS interferograms corresponding to the deformation of a graphite/epoxy composite laminate subjected to an out-of-plane impact at 30 m/s.
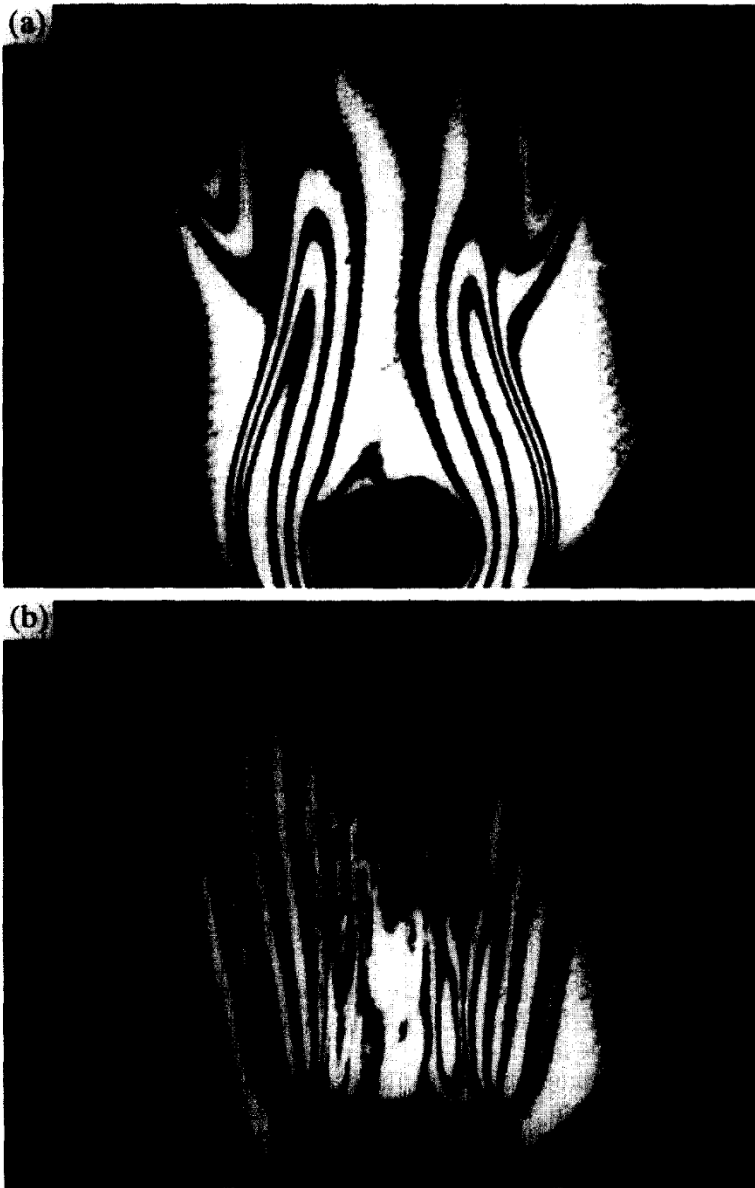
t=5μs t=8.3μs t=10μs t=11.7μs t=13.3μs

t=16.7μs t=18.3μs t=20μs t=21.7μs t=23.3μs

Fig. 12. Fringe pattern obtained by the CGS method from the flame originating from (a) an alcohol burner and (b) a Bunsen burner.

far-field approximation to analyze the entire CGS setup. This analysis is one of the simplest of the existing analyses of CGS. In addition, it is the only one that predicts the interpretation of CGS as contours of equal *difference* of acquired optical path, for large amounts of shearing.

In the second part of the paper we discuss examples of the multifaceted uses of CGS in mechanics. These examples illustrate that CGS is a versatile experimental tool which has already been used successfully in the study of a variety of solid mechanics problems. In particular, the fact that CGS does not suffer from large light intensity losses allows for the use of very small exposure times in dynamic applications, which produces very sharp images of fast-moving subjects.

REFERENCES

1. Bates, W. J., A wavefront shearing interferometer. *Proc. Phys. Soc.*, **59** (1947) 940.
2. Born, M. & Wolf, E., *Principles of Optics,* Pergamon Press, Oxford, 1980.
3. Murty, M. V. R. K., The use of a single plane parallel plate as a lateral shearing interferometer with a visible gas laser source. *Appl. Optics*, **3** (1964).
4. Chao, Y. J., Sutton, M. A. & Taylor, C. E., Interferometric methods for measurement of curvature and twist in thin plates. *Experimental Mech.*, **3** (1982) 531–4.
5. Hariharan, P., Steel, W. H. & Wyant, J. C., Double grating interferometer with variable lateral shearing. *Optics Commun.*, **11** (1974) 317.
6. Hariharan, P. & Hegedus, Z. S., Double grating interferometers II. Application to collimated beams. *Optics Commun.*, **14** (1975) 148.
7. Burger, C. P., Photoelasticity. In *Handbook of Experimental Mechanics,* ed. A. S. Kobayashi. Prentice-Hall, Englewood Cliffs, NJ, 1987, Ch. 5.
8. Rosakis, A. J., Two optical techniques sensitive to gradients of optical path difference: the method of caustics and the coherent gradient sensor (CGS). In *Experimental Techniques in Fracture III,* ed. J. Epstein. 1993, pp. 327–425.
9. Kalthoff, J. F., Shadow optical method of caustics. In *Handbook of Experimental Mechanics,* ed. A. S. Kobayashi. Prentice-Hall, Englewood Cliffs, NJ, 1987, Ch. 9.
10. Parks, V. J., Geometric moiré. In *Handbook of Experimental Mechanics,* ed. A. S. Kobayashi. Prentice-Hall, Englewood Cliffs, NJ, 1987, Ch. 6.
11. Post, D., Moiré Interferometry. In *Handbook of Experimental Mechanics,* ed. A. S. Kobayashi. Prentice-Hall, Englewood Cliffs, NJ, 1987, Ch. 7.
12. Kim, K. S., A stress intensity factor tracer. *J. Appl. Mech.*, **52** (1985) 291–7.
13. Tippur, H. K., Krishnaswamy, S. & Rosakis, A. J., Optical mapping of crack tip deformations using the method of transmission and reflection Coherent Gradient Sensing: A study of crack tip K-dominance. *Int. J. Fracture*, **52** (1991) 91–117.
14. Tippur, H. V., Krishnaswamy, S. & Rosakis, A. J., A coherent gradient sensor for crack tip measurements: Analysis and experimental results. *Int. J. Fracture*, **48** (1991) 193–204.

15. Tippur, H. V., Coherent Gradient Sensing: A Fourier optics analysis and applications to fracture. *Appl. Optics,* **31** (1992) 4428–39.
16. Klein, M. V. & Furtak, T. E., *Optics.* John Wiley, New York, 1986.
17. Mason, J. J., Lambros, J. & Rosakis, A. J., The use of a Coherent Gradient Sensor in dynamic mixed-mode fracture mechanics experiments. *J. Mech. Phys. Solids,* **40** (1992) 641–61.
18. Bruck, H. & Rosakis, A. J., On the sensitivity of coherent gradient sensing: Part I; A theoretical investigation of accuracy in fracture mechanics applications. *Optics and Lasers in Engng,* **17**(2) (1992) 83–101.
19. Bruck, H. & Rosakis, A. J., On the sensitivity of coherent gradient sensing: Part II; An experimental investigation of accuracy in fracture mechanics applications. *Optics and Lasers in Engng,* **18**(1) (1993) 25–51.
20. Rosakis, A. J. & Ravi-Chandar, K., On crack-tip stress states: An experimental evaluation of three dimensional effects. *Int. J. Solids Struct.,* **22** (1986) 121–34.
21. Lee, Y. J. & Rosakis, A. J., Interfacial cracks in plates: A three dimensional numerical investigation. *Int. J. Solids Struct.,* **30** (1993) 3139–58.
22. Krishnaswamy, S., Rosakis, A. J. & Ravichandran, G., On the extent of dominance of asymptotic elastodynamic crack-tip fields: Part II— Numerical investigation of three-dimensional and transient effects. *J. Appl. Mech.,* **58** (1991) 95–103.
23. Rice, J. R., Elastic fracture mechanics concepts for interfacial cracks. *J. Appl. Mech.,* **55** (1988) 98–103.
24. Krishnaswamy, S., Tippur, H. V. & Rosakis, A. J., Measurement of transient crack tip deformation fields using the method of Coherent Gradient Sensing. *J. Mech. Phys. Solids,* **40** (1992) 339.
25. Tippur, H. V. & Rosakis, A. J., Quasi-static and dynamic growth along bimaterial interfaces: A note on crack-tip field measurements using Coherent Gradient Sensing. *Experimental Mech.,* **31** (1991) 243–51.
26. Lambros, J. & Rosakis, A. J., Dynamic decohesion of bimaterials: Experimental observations and failure criteria. *Int. J. Solids Struct.,* **32** (1995) 2677–702.
27. Lambros, J. & Rosakis, A. J., Transonic crack growth in bimaterials—Part I: Experimental observations. *J. Mech. Phys. Solids*, **43** (1995) 169–88.
28. Lambros, J. & Rosakis, A. J., On the development of a dynamic decohesion criterion for bimaterials. *Proc. Roy. Soc. Lond. Series A.,* to appear.
29. Lambros, J., Rosakis, A. J. & Karyaclis, M., Dynamic failure of composite structures. Paper presented at 12th National Congress, Seattle, July 1994.